GSA DATA REPOSITORY 2015060

WFSD1 Temperature Profiles.zip

Supplementary Information

Title of manuscript: Long-term Temperature Records following the M_w 7.9 Wenchuan Earthquake Consistent with Low Friction

Haibing Li[1]*, Lian Xue[2], Emily E. Brodsky[2], James Mori[3], Patrick M. Fulton[2], Huan Wang[1], Yasuyuki Kano[3], Kun Yun[1], Robert N. Harris[4], Zheng Gong[1], Chenglong Li[1], Jialiang Si[1], Zhiming Sun[5], Junling Pei[5], Yong Zheng[1] and Zhiqin Xu[1],

[1]*State Key Laboratory of Continental Tectonics and Dynamics, Institute of Geology, Chinese Academy of Geological Sciences, Beijing, China*

[2]*Department of Earth & Planetary Sciences, University of California–Santa Cruz, Santa Cruz, California 95064, USA*

[3]*Disaster Prevention Research Institution, Kyoto University, Gokasho, Uji, Kyoto, Japan*

[4]*Oregon State University, Corvallis, Oregon 97331, USA*

[5]*Institute of Geomechanics, Chinese Academy of Geological Sciences, Beijing, China*

*Correspondence to: lihaibing06@163.com

Profile Alignment

The approximate depth of measurement was known from the pressure transducers on the logs and an independent measurement of water level in the well. Converting pressure to depth requires an estimate of the water density. Since the actual well water density is different from the pressure transducer manufacturer's default water density of 1.0281×10^3 kg/m^3, we made a correction for the water density by comparing the known winch vertical length and the record vertical depth of the pressure transducers of the three high-precision stop-go logs. The range of resulting densities is 1.0035-1.0055×10^3 kg/m^3, so we used the average value of 1.0052×10^3 kg/m^3 as the water density to correct the pressure transducer depths for all the profiles.

However, pressure accuracy (and occasional failure), uncertainty in water level and variations of well fluid density made an additional alignment procedure necessary. We therefore aligned the temperature profiles based on identifying short-wavelength features and gradient changes in the temperature profiles related to sharp contrasts in the gamma-ray logs and recovered cores (Figs. DR 1 and DR 2). We initially aligned the profiles on the 394 m boundary and then checked the results by identifying features on the other known boundaries (Fig. DR 2). The consistency of the 589 m and 700 m features across the profiles is a useful check on the alignment procedure.

The individual profile temperature data is included as a matlab structure WFSD1TemperatureProfiles in the data repository of this article. For each profile, the fields: raw vertical depth as measured by the pressure transducer (PressureTransducerDepth), vertical depth that includes corrections for water density and alignment (VerticalDepth), borehole depth that includes inclination correction (CorrectedDepth) and the starting date of the log (LoggingStartTime).

Thermal Conductivity

Frictional heating on fault surfaces is manifested in temperature-depth profiles as small perturbations to the background thermal regime. Before interpreting perturbations as frictional heating it is important to remove other sources of perturbations. In borehole WFSD-1 a primary source of perturbations are caused by variations in thermal conductivity. The analysis that follows is a conservative approach in that we strive to minimize perturbations while honoring the data.

Thermal conductivity was measured on the WFSD-1 core at 121 locations by an optical scanning technique using an apparatus manufactured by Lippmann Geophysical Instruments (Popov et al., 1999). This apparatus has a reported accuracy of ±3% in the range between 0.2 and 25 W $m^{-1}K^{-1}$. This system uses a focused, continuous, and mobile heat source to heat the surface while an infrared temperature sensor lags behind at a constant interval and measures excess temperature. The determination of thermal conductivity values is based on the comparison of excess temperatures to that of reference samples with a known thermal conductivity (Popov et al., 1999). Sample preparation consisted of choosing samples that minimized surface roughness and painting that surface with a thin coat of nitrolacquer to counteract optical reflectivity. Within the fault zone where core surfaces were very rough samples were polished. Measurements were made under dry conditions with a scan rate of 5 mm/s. Thermal conductivity was measured at every 5 m between depths of 350 and 800m and was supplemented with denser, 1 m sampling between depths of 570 and 610 m (Fig. DR 4).

Measured dry values of thermal conductivity vary between approximately 1 and 4 $Wm^{-1}K^{-1}$ (Fig. DR 4) and have been have been sorted on the basis of their lithology (Li et al., 2013). These values generally agree with values reported in the literature (e.g., Kappelmeyer and Haenal, 1974). Typical values of volcaniclastics and diorite are reported to be 2.2 and 3.5 W/m/K. The interbedded sandstones and dark fine sandstones show the largest variation with values between 1 and 4 W/m/K. The massive sandstones show relatively low values between 1.5 and 2.5 W/m/K, and the fault zone rocks also characterized as mixed sandstone. The low values of the sandstone likely reflect a systematic bias due to higher porosities because thermal conductivities were measured under dry conditions whereas the in-situ condition is saturated.

We derive an estimate of thermal conductivity values for saturated conditions as follows. We divide thermal conductivity values into lithological units by following Li et al. (2013) and note discontinuities in measured thermal conductivity values from laboratory analysis of the core. Maximum and mean core thermal conductivity values for each unit are reported in Table DR 1 and Fig. DR 5. The maximum value for each unit is assumed to represent samples with the lowest porosity (i.e., closest to a matrix value) and therefore is closest to in-situ thermal conductivity. We then determine the value of heat flow over the interval 350 to 800 m that minimizes the difference between the maximum laboratory measurement of conductivity and the inferred value that linearizes the observed thermal gradient. This procedure ascribes differences between the mean and maximum value of thermal conductivity to the porosity while also minimizing the inferred porosity. Thermal gradients for each unit are estimated by fitting the top and bottom 5 temperature measurements for the unit instead of a least-squares fit of all the data. This procedure is better at preserving any internal temperature features within the unit as seen in the anomaly centered over ~700 m depth. The resultant values of heat flow for the different logs range from 69 to 72 mW/m^2, which is consistent with regional heat flow at this site on the margin of the Tibetan plateau and the Sichuan basin (Xu et al., 2011). Based on the inferred heat flow and the measured gradients, we solve for the conductivity in each unit (Fig. DR4).

As a check on this procedure, we also calculate the porosity assuming that the current measurements are completely dry and the inferred in-situ values are saturated, i.e., if the bulk field thermal conductivity is

$$\sqrt{\lambda_B} = \phi\sqrt{\lambda_w} + (1-\phi)\sqrt{\lambda_m} \qquad \text{(S1)},$$

where λ_B is the bulk thermal conductivity, ϕ is the porosity, λ_w is the thermal conductivity of water and λ_m is the matrix thermal conductivity (Beardsmore and Cull, 2001).

In the laboratory measurements, the air-filled pore space has negligible thermal conductivity and therefore

$$\sqrt{\lambda_B} = \phi\sqrt{\lambda_w} + \frac{1-\phi}{1-\phi_{lab}}\sqrt{\lambda_{lab}} \qquad \text{(S2)},$$

where λ_{lab} is the measured thermal conductivity in the laboratory and ϕ_{lab} is the laboratory porosity. We assume that the change of porosity with confining pressure is sufficiently small that $\frac{1-\phi}{1-\phi_{lab}}$ is approximately 1. This approximation is adequate for the moderate effective pressures (<10 MPa) in this borehole. For instance, in compaction experiments of Chen et al. (2013) on Wenchuan fault zone gouge from an exposed outcrop, the predicted porosity changes at 10 MPa is <1%. We solve for the porosity ϕ for each profile by assuming λ_B is the fit value for the unit from the optimization procedure described above, λ_{lab} is the mean laboratory-derived value of the unit, and thermal conductivity of water is 0.6 $Wm^{-1}K^{-1}$.

The inferred thermal conductivity structure and porosity is shown in Fig. DR 4 for each profile. As can be seen, the porosity is always positive, as required physically, and is highest in the sandstone units where high porosity is expected, and has generally reasonable values at all depths. The results are consistent across all profiles suggesting that the procedure is robust.

Once the conductivity structure is determined, we use the Bullard (1939) method to extract anomalous temperatures relative to the background conductive geotherm. In this method the predicted temperature T(z), at depth, z, may be expressed as,

$$T(z) = T_o + q_o \sum_{i=1}^{N} \frac{\Delta z_i}{k(z)_i} \qquad \text{(S3)}$$

where $k(z)_i$ is the thermal conductivity measured over the i^{th} interval Δz_i, and the summation is performed over N intervals that span the depth of interest. The parameters q_o and T_o are estimated by plotting $T(z)$ against summed thermal resistance $\Sigma \Delta z_i / k(z)_i$ Anomalous temperatures are computed as the difference between the observed and predicted background temperatures.

Alternative unit layer structure

This procedure to identify thermal anomalies is sensitive to the layer boundaries inferred from the logging and core data. It is notable that the two largest anomalies in Fig. 3 occur in areas where no lithological boundaries were inferred. We therefore repeated the analysis with an additional layer boundary in the middle of the largest anomaly to test the sensitivity of the results to the structure.

Figs. DR 5 and DR 6 are analogous to main text Fig. 3 and Fig. DR 4 with an additional boundary at 693 m. This depth has a prominent change in the gamma ray log variability and individual fault gouges are closely spaced above this level. However, the host rock is the same on both side of 693 and the mean value of laboratory measurements of thermal conductivity does not show any strong discontinuity here therefore we did not include the boundary in our preferred model.

The anomalous temperature at 700 m is greatly reduced by the additional boundary for all profiles and therefore the maximum bound on the coseismic dissipated heat energy is lower for this model. In addition, a smaller, negative anomaly above the 693 boundary decays with time. The decay is consistent with the gradient increasing as the borehole re-equilibrates from the drilling perturbation. The inferred porosities for this model exceed 80% in the layer below 693 m, which is likely an unphysical value.

We infer that the fundamental conclusions of this paper are unchanged by the existence of a 693 m boundary. A conductively diffusing, positive heat anomaly is still not observed and the dissipated thermal energy is still significantly below the upper bound in the main text (29 MJ/m^2). We also infer that a thermal conductivity boundary at

693 m is unlikely based on the laboratory thermal conductivity measurements and the high requisite porosity.

Frictional Heat Model

We model the residual temperature due to the dissipation of frictional energy *S* on a plane as a plane source of heat diffusing into a layered medium with the conductivity structure as determined from the Bullard plot inversion (Fig. DR 7). We use a 1-D finite difference calculation to diffuse the heat from the fault plane into the surrounding layers, which are assumed to be parallel to the fault and inclined at an angle of 45° to the borehole (The fault dips 55° and the borehole is incline 10°). The initial conditions of the calculation are set using the analytical solution in a homogeneous medium at time Δt after the earthquake where Δt is the timestep of the rest of the calculation. For the results presented here Δt=1250 s.

$$\Delta T_{EQ}(\hat{z},t) = \frac{S}{2\sqrt{\pi\alpha_0\Delta t}} e^{-(\hat{z}-\hat{z}_f)^2/4\alpha_0\Delta t} \qquad \text{(S4)}$$

where *S* is the dissipated energy on the fault plane z_f, z is the coordinate direction normal to the plane, and α_0 is the thermal diffusivity closest to the fault. After the first time step, the full thermal conductivity structure as constrained by the constant heat flow inversion is employed. For simplicity, we select the thermal conductivity structure inverted from one of the best resolved profiles, which is from Dec. 30, 2012. As can be seen from Fig. DR 4, the inverted structure is substantially similar for all the profiles.

For the full suite of inverted profiles, S_{450}=5 +/- 2 and S_{690}=24+/-6. These two anomalies are superposed in Fig. 3b.

The Drilling Anomaly

The observed temperature gradient steepens with time (Fig. 1). This steepening is expected for the recovery of the borehole from the drilling anomaly. Drilling itself significantly perturbs the geotherm. Standard drilling procedure is to circulate mud continuously in the borehole at a constant temperature at a rate of about 0.1 m^3/min. This constant circulation is designed to maintain borehole pressure, circulate out drill cuttings and advect away the frictional heat generated by the drill bit (Lachenbruch and Brewer, 1959). Therefore, the drilling effect is well-modeled by an isothermal line source of duration equal to the drilling time (Fulton et al., 2010; Lachenbruch and Brewer, 1959; Bullard, 1947; Jaeger, 1961; Herzen and Scott, 1991).

The drilling team did not record the mud temperature in WFSD-1, but the range of mud temperatures directly recorded in the nearby WFSD-2 is 21-26.6^{o}. (WFSD-2 is not suitable for fault zone temperature measurements because of its complex and prolonged drilling history). We assume that a similar range was used by in WFSD-1 and calculate the drilling anomaly at the 589 m fault where we are studying the smallest feature.

For a conductively cooling system, the line source imposes a cylindrical symmetry that results in a faster decay than the planar source of the fault heating anomaly. Specifically, the temperature anomaly from drilling at time t since the beginning of drilling at a particular depth is

$$T/T_0 = \log(1 + t_1/(t- t_1)) /(\log(4\, \kappa t /a^2) -0.577) \qquad \text{(S5)}$$

where T_0 is the difference between drilling mud temperature and the original temperature at a particular depth, κ is the thermal diffusivity, t_1 is the duration of drilling at that depth, and a is the wellbore radius. (Bullard, 1947, Eq. I). Eq. S5 is used with the drilling history to calculate the positive temperature anomaly associated with the range of possible fluid temperatures. The range of positive anomalies possible at the 589 fault is shown by the gray shaded area in Fig. DR 7.

In contrast, the conductive temperature decay of a planar fault is

$$T=(\mu\, \sigma_n\, d/c_p) \,/\, (2\,(\pi\, \kappa\, t)^{1/2}) \qquad \text{(S6)}$$

where μ is the coefficient of friction, σ_n is the effective normal stress, d is the slip, c_p is the specific heat capacity and κ is the thermal diffusivity (Carslaw and Jaeger, 1959). For typical values of these parameters, there is expected to be a cross-over time at which the fault heating dominates over the drilling anomaly (Fig. DR 7). Therefore, a fault zone heating signal can potentially be significant after the drilling anomaly decays.

Lithology	Top (m)	Bottom (m)	Mean λ_{lab} (W/m/K)	Max λ_{lab} (W/m/K)	Model Fit λ(W/m/K)
Volcanic	349	363	2.34	2.58	3.50
Diorite	363	394	3.19	4.21	3.45
Volcanic	394	494	2.65	3.83	3.33
Diorite	494	512	2.29	2.62	3.57
Volcanic	512	545	3.14	3.58	3.58
Diorite	545	555	2.56	2.79	3.42

Volcanic	555	576	2.96	3.90	3.36
Cataclasite	576	585	2.50	3.02	3.18
Fault breccia	585	595	1.76	3.29	2.95
Siltstone	595	759	1.91	3.40	3.13
Sandstone	759	800	3.30	3.84	3.41

Table DR 1.

Thermal conductivity structure. Unit boundaries determined from Li et al. (2013) and Li. et al. (2014). The alternative interpretation in Figs. DR 5- DR 6 has an additional boundary at 693 m depth that separates the highly faulted sandstone from the lower, more homogeneous unit. Model fit is the mean of the fits for all of the profiles for the given unit.

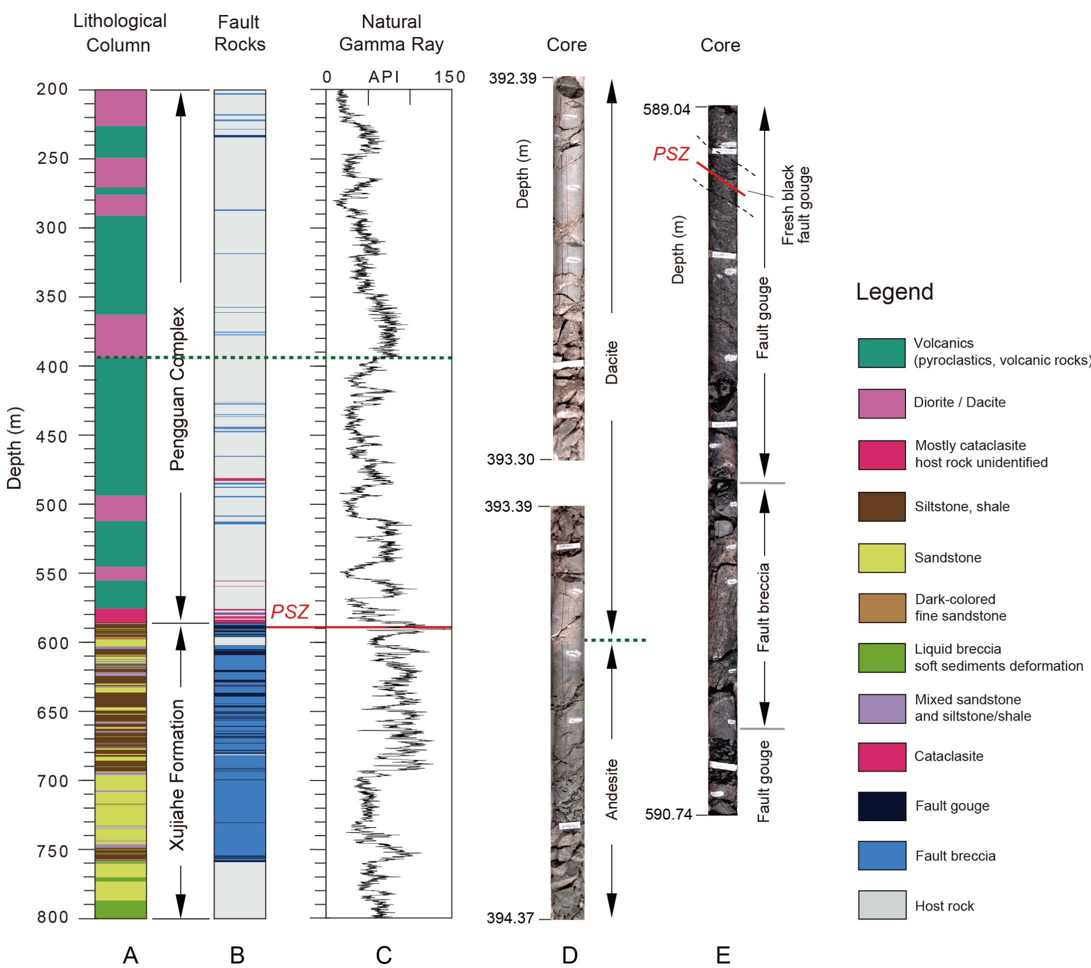

Figure DR 1

Lithological column, logging and core images constraining two key contacts: the lithological contact between dacite and andesite at 394 m core depth, and the potential principal slip zone at 589 m core depth. The first contact 394 m is selected as one of the clearest sharp features in the logging and temperature data that is far from the fault zone. It therefore provides control on the alignment of the depth of the temperature logs.

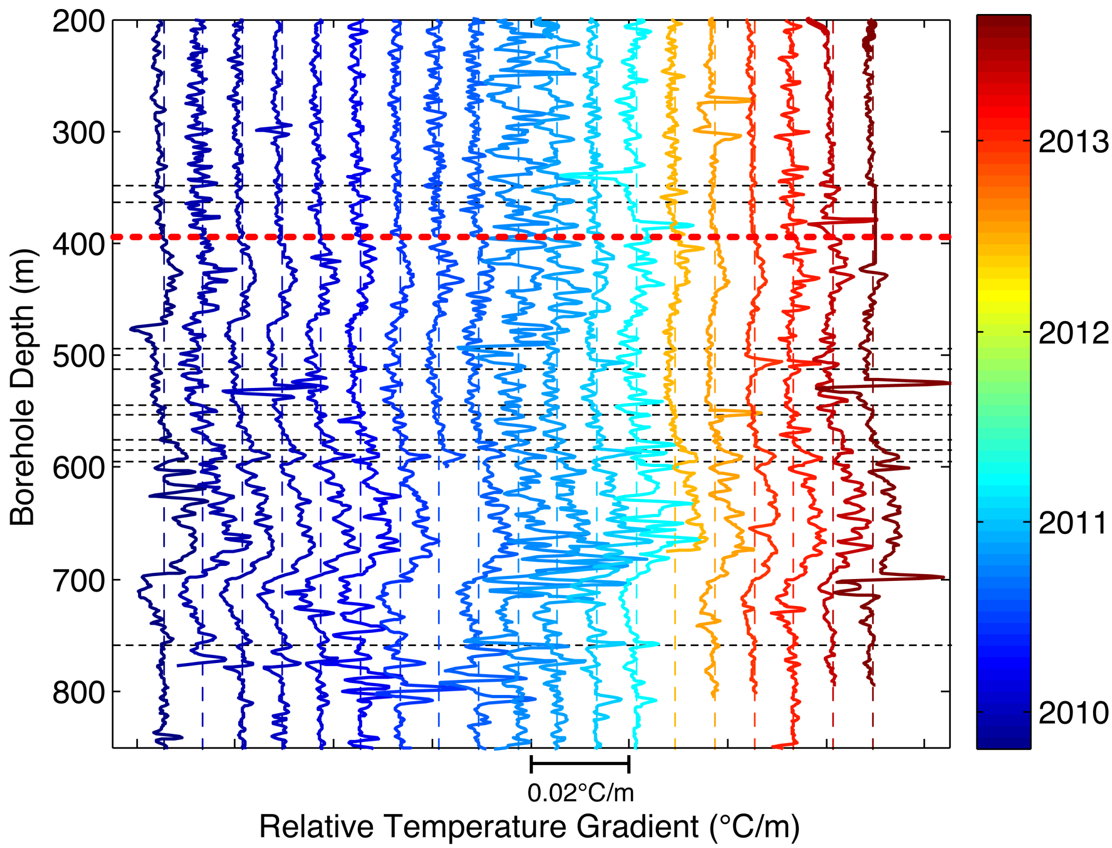

Figure DR 2

Depth variation in temperature gradient for each temperature profile. Profiles are shifted along the x-axis to allow each profile to be seen individually. The high-frequency features are aligned on the known lithological boundary at 394 m using these differential temperature (gradient) profiles. Color scale indicates logging time and is identical to all other figures of the paper.

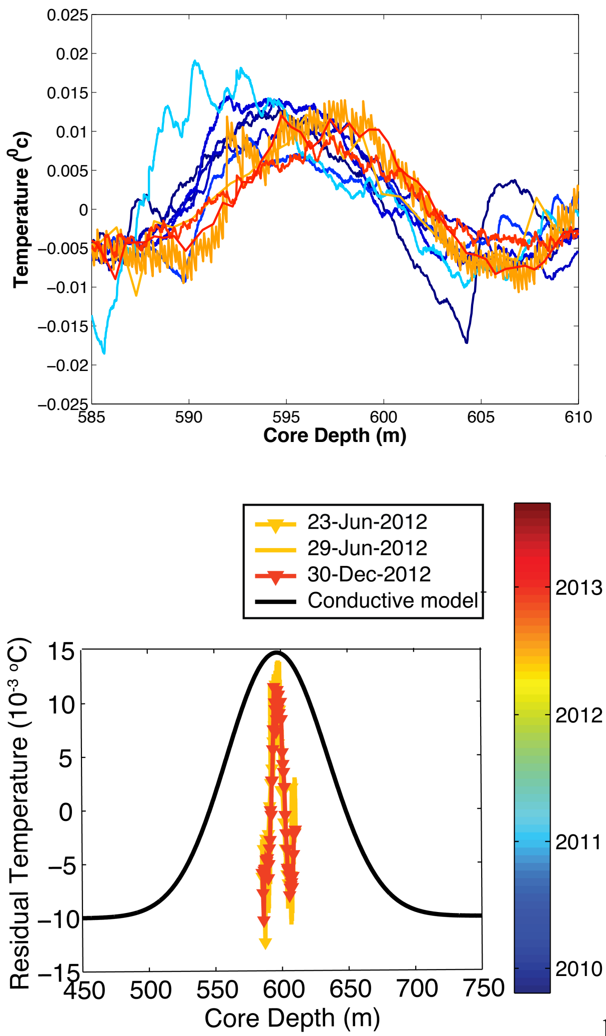

a

b

Figure DR 3

View of the 590 m fault zone anomaly (a) Close-up of fault zone anomaly for the least noisy records. Colors correspond to dates as in the colorbar in Fig. DR 2. (b) Comparison of anomaly and a calculated frictional anomaly with shear stress set to match observed amplitude and diffusion time equal to the time between the earthquake and the observation. The calculated diffusive anomaly is wider than observed.

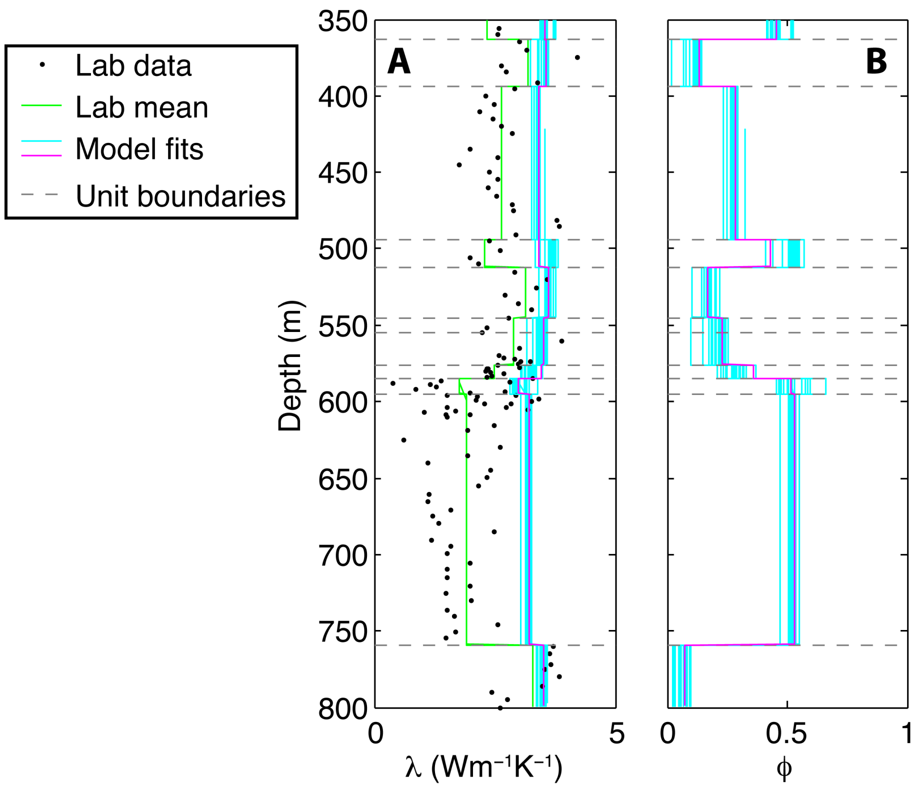

Figure DR 4

Thermal conductivity (λ) and inferred porosity as a function of depth. (A) Dots indicate laboratory measurements of thermal conductivity on the recovered core. The lab mean is a thermal conductivity structure model that takes the mean of the lab measurements in each geological unit bounded by the dashed lines. For each profile, we invert a model fit conductivity structure (cyan lines) that is constrained to have a constant heat flow over all the units with the observed gradients while minimizing the difference between the model fit and the maximum of the thermal conductivity in each unit. Magenta line distinguishes one model fit so fine-structure can be examined. (Magenta is 30 December, 2012 stop-go profile). (B) Porosity computed with Eq. S2 for the model fits in (A).

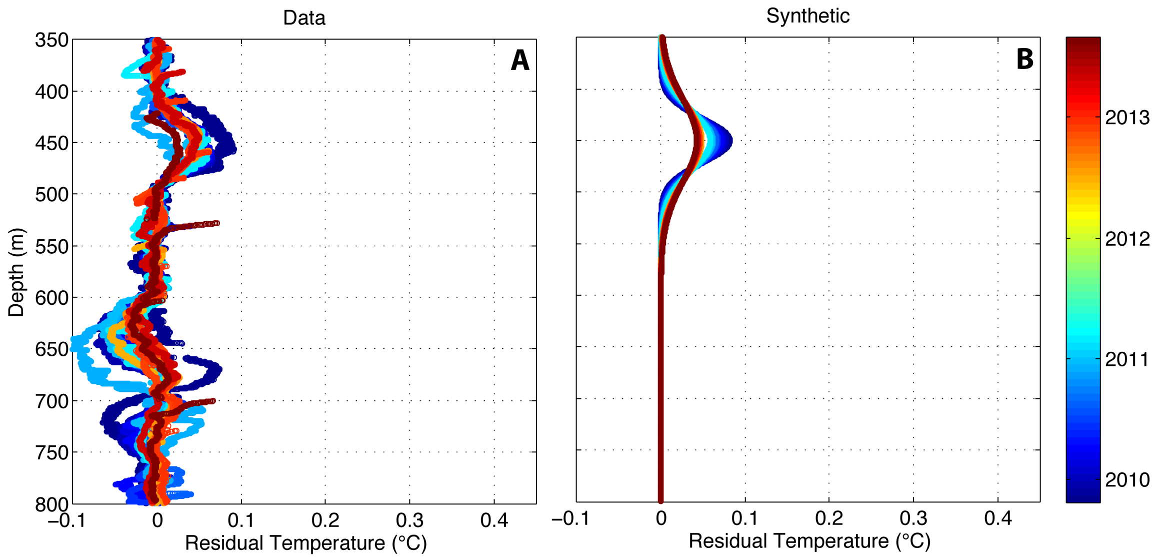

Figure DR 5

Residual (anomalous) temperature after the conductive geotherm is removed for the alternative model with an extra unit boundary at 693 m depth (a) Observed residual temperature for each profile color-coded by date. The thermal conductivity is as in Fig. DR 6. (b) Modeled residual temperature for frictional dissipation on 450 m surfaces with the total dissipated energy constrained to be equal to the observed residual thermal energy (See Supplementary Information text). The frictionally dissipated energy is transported from the fault zone by diffusion. For this alternative thermal model, no positive temperature anomaly is observed at 700 m depth, therefore no frictional heat was modeled there.

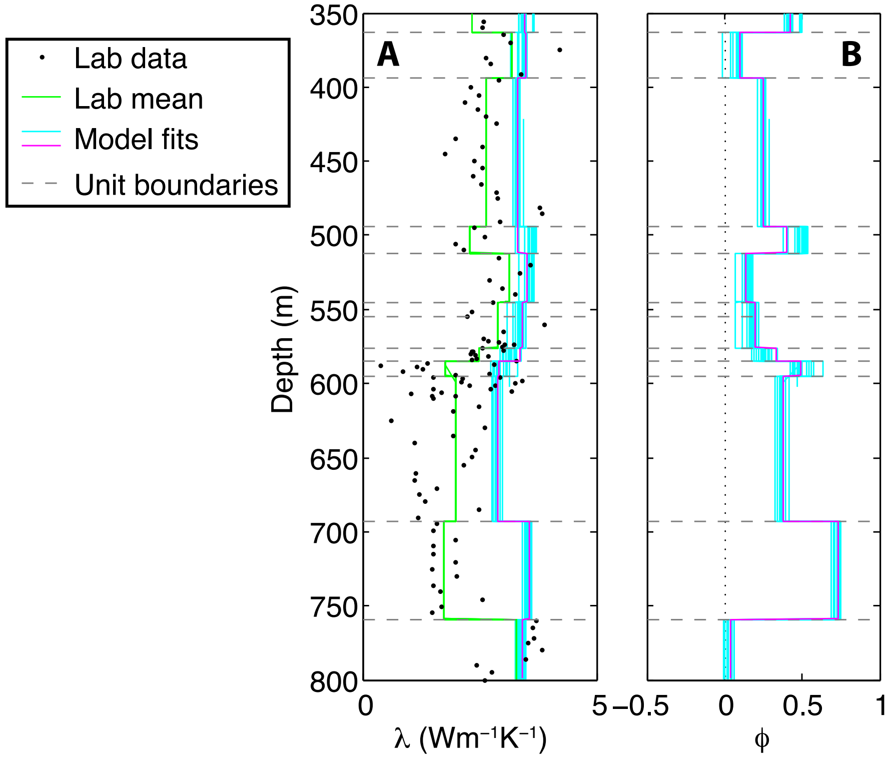

Figure DR 6

Thermal conductivity (λ) and inferred porosity as a function of depth for the alternative model with an extra unit boundary at 693 m depth. (A) Dots indicate laboratory measurements of thermal conductivity on the recovered core. The lab mean is a thermal conductivity structure model that takes the mean of the lab measurements in each geological unit bounded by the dashed lines. For each profile, we invert a model fit conductivity structure (cyan lines) that is constrained to have a constant heat flow over all the units with the observed gradients while minimizing the difference between the model fit and the maximum of the thermal conductivity in each unit. Magenta line distinguishes one model fit so fine-structure can be examined. (Magenta is 30 December, 2012 stop-go profile). (B) Porosity computed with Eq. S2 for the model fits in (A).

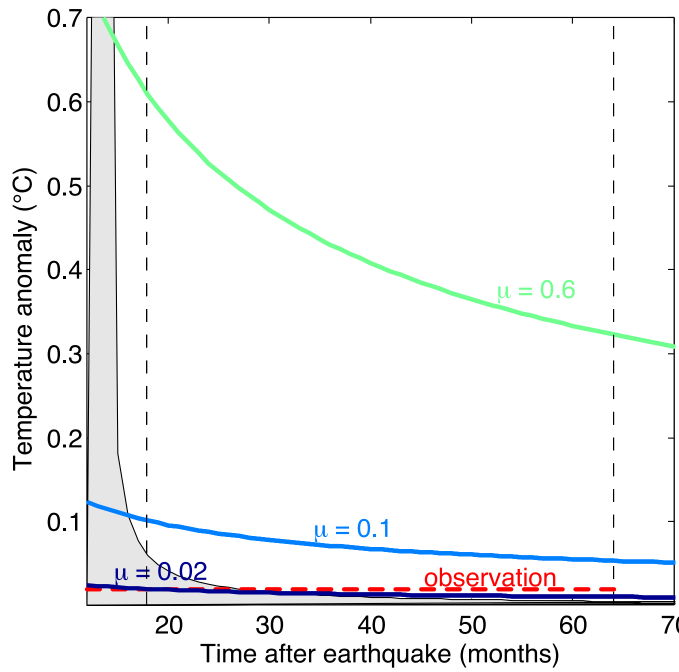

Figure DR 7

Predicted maximum amplitude of the temperature anomaly for the fault in the WFSD-1 borehole with representative effective co-seismic coefficients of friction. Dashed lines show the first and last measurement time and the maximum temperature anomaly at the fault crossing is shown by the red dashed line. Temperature curves are computed from the planar fault model in Equation 2 of the main text with $\sigma_n = 9$ MPa, $c_p = 800$ J/kg (Beardsmore and Cull, 2001),ρ=2500 (Li et al., 2014), $d = 7$ m, and $\kappa = 1.5 \times 10^{-6} m^2/s$. A simplified model for the normal stress as equal to the lithostatic overburden less the hydrostatic pore pressure is used in lieu of independent constraints on the deviatoric stress on this reverse fault. Although this simplification introduces less error than the uncertainty on slip, it is important to bear in mind when comparing this apparent friction here to any other data set. Grey region shows the predicted drilling anomaly at 589 m depth for a range of drilling mud temperatures up to a 26.6^{o}C. Flat top of this region indicates time drilling.

REFERENCES CITED

Beardsmore, G.R., and Cull, J.P., 2001, Crustal heat flow: a guide to measurement and modelling. Cambridge,UK: Cambridge Univ. Press.

Bullard, E. C., 1939, Heat Flow in South Africa. *Proceedings of the Royal Society a: Mathematical*, *Physical and Engineering Sciences*, 173(955), 474–502. doi:10.1098/rspa.1939.0159

Bullard, E., 1947, The time necessary for a bore hole to attain temperature equilibrium： Geophysical Journal International, v. 5, p. 127–130, doi:10.1111/j.1365-246X.1947.tb00348.x.

Carslaw, H. S., and Jaeger, J. C., 1959, Conduction of heat in solids. -1, (Oxford: Clarendon Press, 1959, 2nd ed., 1959).

Chen, J., Yang, X., Yao, L., Ma, S. & Shimamoto, T. Frictional and transport properties of the 2008 Wenchuan Earthquake fault zone: Implications for coseismic slip-weakening mechanisms. *Tectonophysics* **603,** 237–256 (2013)

Fulton, P. M., Harris, R. N., Saffer, D. M., and Brodsky, E. E., 2010, Does hydrologic circulation mask frictional heat on faults after large earthquakes? : Journal of Geophysical Research, v. 115, B09402, doi:10.1029/2009JB007103.

Herzen, von, R., and Scott, J., 1991, Thermal Modeling for Hole 735B1: Proceedings of the Ocean Drilling Program: Scientific Results, v. 118, p. 349–356.

Jaeger, J., 1961, The effect of the drilling fluid on temperatures measured in bore holes: Journal of Geophysical Research, v. 66, p. 563–569, doi: 10.1029/JZ066i002p00563.

Kappelmeyer, O. and R. Haenel, 1974, *Geothermics with special reference to application*, Berlin: Gebrueder Borntraeger (Geoexploration Monographs. Series 1, No. 4).

Lachenbruch, A., and Brewer, M., 1959, Dissipation of the temperature effect of drilling a well in Arctic Alaska: United States Geological Survey Bulletin, v. 1083, p. 73–109.

Li, H., and 11 others, 2013, Characteristics of the fault-related rocks, fault zones and the principal slip zone in the Wenchuan Earthquake Fault Scientific Drilling Project Hole-1 (WFSD-1): Tectonophysics, v. 584, p. 23-42, doi:10.1016/j.tecto.2012.08.021

Li, H., and 11 others, 2014, Structural and physical properties characterization in the Wenchuan earthquake Fault Scientific Drilling project-hole 1 (WFSD-1): Tectonophysics, v. 619, p. 86-100, doi:10.1016/j.tecto.2013.08.022.

Melosh, H. J., 1979, Acoustic Fluidization - New Geologic Process: Journal of Geophysical Research, v. 84, p. 7513–7520, doi:10.1029/JB084iB13p07513.

Popov, Y.A., Pribnow, D.F.C., Sass, J.H., Williams, C.F., and Burkhardt H., 1999, Characterization of rock thermal conductivity by high-resolution optical scanning, Geothermics, v. 28, p. 253–276.

Xu, M., Zhu, C.Q., Tian, Y.T., Song, Rao, S., and Hu, S.B., 2011, Borehole temperature logging and characteristics of subsurface temperature in the Sichuan Basin: Chinese Journal of Geophysics, v. 54, p. 224–233, doi:10.1002/cjg2.1604.